Konrad-Zuse-Zentrum
für Informationstechnik Berlin

Takustraße 7
D-14195 Berlin-Dahlem
Germany

C. KOBER[1] B. ERDMANN J. LANG
R. SADER H.–F. ZEILHOFER

Adaptive Finite Element Simulation of the Human Mandible Using a New Physiological Model of the Masticatory Muscles

[1]An abstract of this article (2 pages) has been submitted to the Proceedings of the 75th Annual Meeting of the GAMM, March 21-27, 2004, Technical University of Dresden, Germany

ZIB-Report 04-16 (June 2004)

Adaptive Finite Element Simulation of the Human Mandible Using a New Physiological Model of the Masticatory Muscles

Cornelia Kober[1,5] Bodo Erdmann[2] Jens Lang[3]
Robert Sader[4,5] Hans–Florian Zeilhofer[4,5]

Abstract

Structural mechanics simulation of bony organs is of general medical and biomechanical interest, because of the interdependence of the inner architecture of bone and its functional loading already stated by Wolff in 1892.

This work is part of a detailed research project concerning the human mandible. By adaptive finite element techniques, stress/strain profiles occurring in the bony structure under biting were simulated. Estimates of the discretisation errors, local grid refinement, and multilevel techniques guarantee the reliability and efficiency of the method.

In general, our simulation requires a representation of the organ's geometry, an appropriate material description, and the load case due to teeth, muscle, or joint forces. In this paper, we want to focus on the influence of the masticatory system. Our goal is to capture the physiological situation as far as possible. By means of visualization techniques developed by the group, we are able to extract individual muscle fibres from computed tomography data. By a special algorithm, the fibres are expanded to fanlike (esp. for the musculus temporalis) coherent vector fields similar to the anatomical reality. The activity of the fibres can be adapted according to compartmentalisation of the muscles as measured by electromyological experiments. A refined sensitivity analysis proved remarkable impact of the presented approach on the simulation results.

[1]Fac. of Engineering and Computer Science, Univ. of Appl. Sc. Osnabrück, Germany
[2]Zuse Institute Berlin, Germany
[3]Institute for Mathematics, Darmstadt University of Technology, Germany
[4]University Hospital Basle, Switzerland
[5]Center of Adv. Studies in Cranio-Maxillo-Facial Surgery, Munich Univ. of Techn., Germany

1 Introduction

Severe changes of the human mandible during lifetime, see Figure 1, stimulated a lot of medical and biomechanical research in this field. Three dimensional simulation of the human mandible by finite element methods had its beginning in the early nineties of the last century. Among the pioneers were Korioth [19] and Hart [11]. In the meantime, a rich body of literature is available. We refer to [25] for a review on mandibular biomechanics.

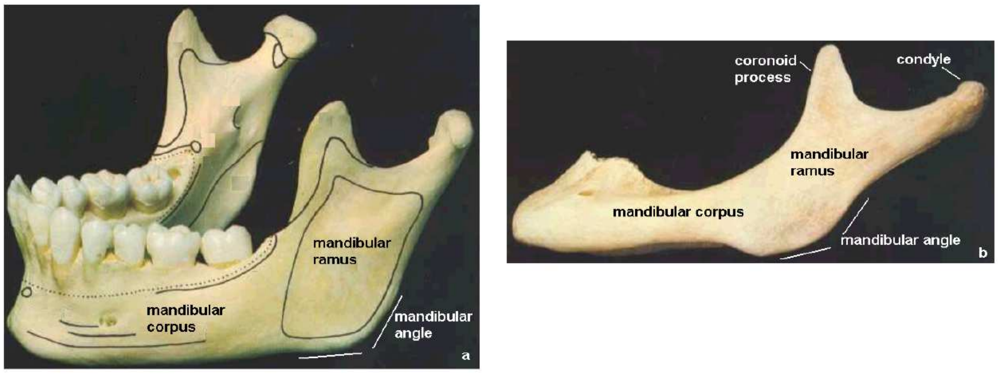

Figure 1: Mandible at adulthood (a) and at senium (b).

The work presented in this article is part of an interdisciplinary project concerning this bony organ. It ranges from numerical mathematics over biomechanical modelling to medical application.

The correlation of the inner architecture of bone and its functional loading was already stated by Wolff in 1892 [27]. Our objective is to demonstrate this interdependence for the human mandible. By adaptive finite element techniques, stress/strain profiles occurring at human biting were simulated. Additionally, by a combination of computer graphics modules [17], a three dimensional volumetric visualization of bone mineral density could be given, see Figure 2. For a more detailed introduction to this approach, see [15].

In general, our simulation requires a representation of the organ's geometry, an appropriate material description, and a realisation of the load case due to teeth, muscles, or joint forces. This paper is focused on individual modelling the masticatory system and its influence on the simulation results. The masticatory system comprises the masseter muscles, the two temporals, the medial, and the lateral pterygoids. Furthermore, the authors studied the impact of the underlying numerical concept of adaptive finite elements on the significance of the simulation results.

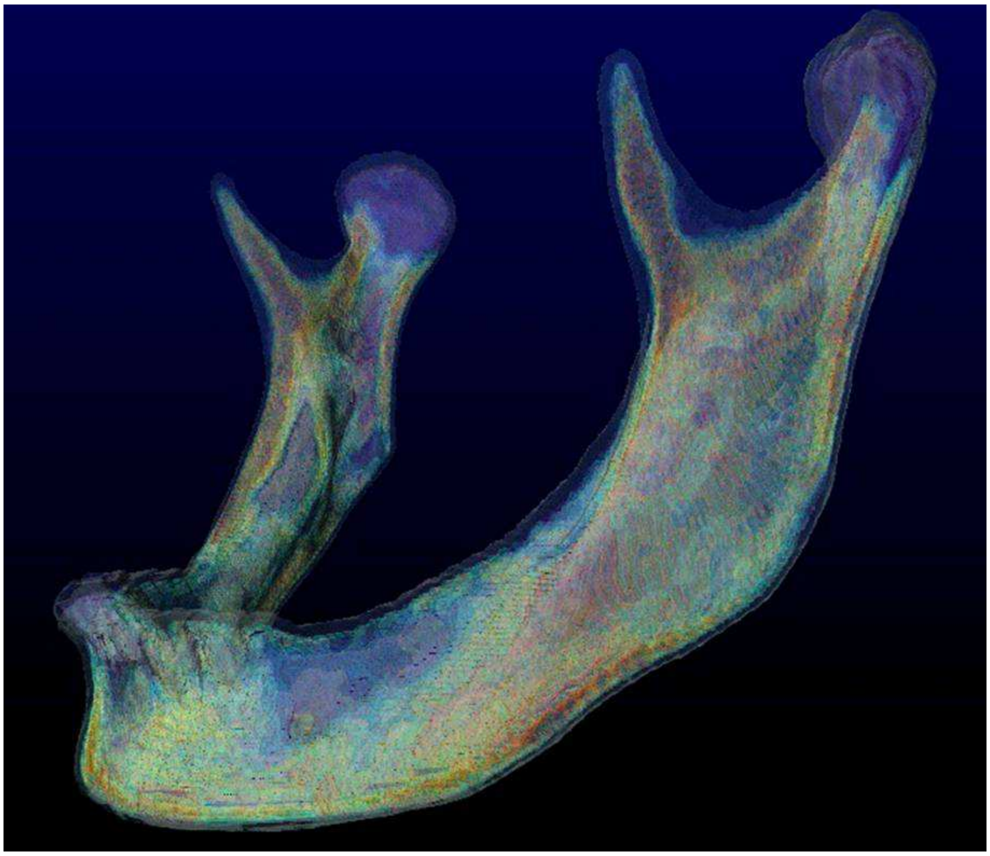

Figure 2: Three dimensional visualization of the inner structure of the cortical shell of the mandible [17].

The paper is organized as follows. Within the first paragraph of the next section, a short outline of the prerequisites of the simulation is given. The subsequent paragraph is dedicated to a description of the numerical background. The section is completed by a description of the modelling of the masticatory muscles. In Section 3, we give a general depiction of some simulation results and report a detailed sensitivity analysis with respect to adaptive grid refinement and the choice of the muscular "lines of action" representing the directions of muscle activity. Based on these results, a conclusion will be drawn in Section 4 combined with a short discussion. Finally, the article is closed by an outlook to future and ongoing activities within our project, and an acknowledgement.

2 Materials and Methods

2.1 Short outline of the prerequisites of the simulation

As mentioned above, the prerequisites of the simulation consist of an acceptable representation of the organ's geometry, an appropriate material description, and a realisation of the load case due to teeth, muscles, or joint forces.

Because of its beginning atrophy of the alveolar ridge, the disposability of multimodal data sets including CT–data (CT: computer tomography), MRT–data (MRT: magnetic resonance tomography), and anatomical photographs, we chose the mandible of the female Visible Human as simulation example [3].

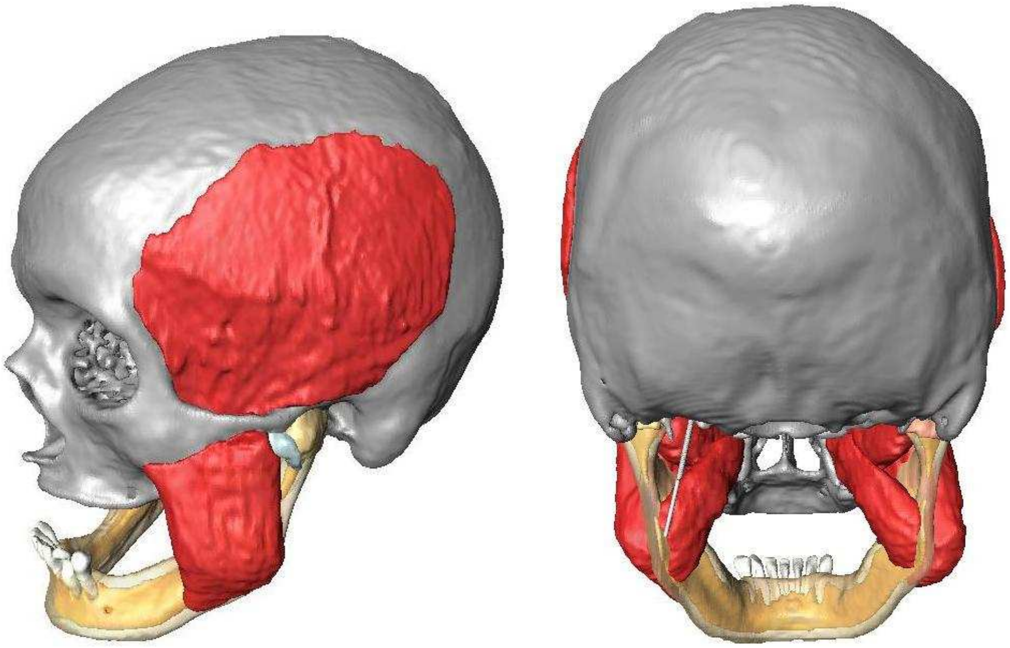

Figure 3: Geometry representation.

The reconstruction of the individual craniofacial anatomy, see Figure 3, was performed by a superposition of the CT-data and the anatomical photographs [16]. The skull, the cortical shell of the mandible, its inside spongy bone, the teeth, the masticatory system (musc. masseter, temporales, pterygoidei mediales, pterygoidei laterales), and two simplified temporo mandibular joint capsules are separated geometric entities. For further steps as finite element mesh generation, we refer to [9].

In spite of the ability of anisotropic simulation of the jaw bone, see [13], we refrained from those techniques in this setting. So, we chose an isotropic material law and assumed piecewise homogeneity for all involved materials (cortical and cancellous bone separated). According to [9], we set an average Young modulus E = 13.3 GPa for cortical, E = 1.33 GPa for spongy bone, and E = 16.0 GPa for the teeth. The Poisson ratio is assumed to be 0.224 for both constituents of bone and for the teeth.

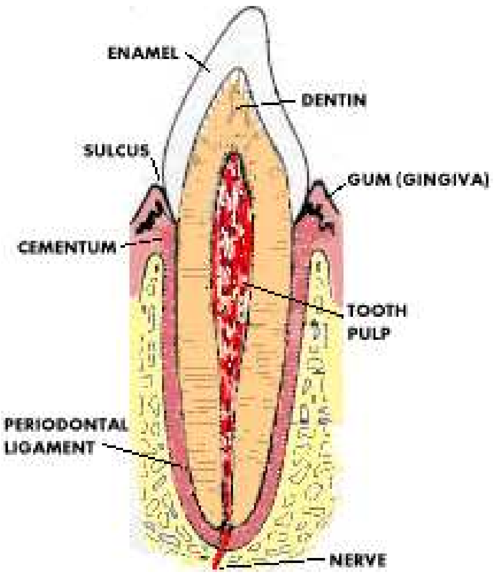

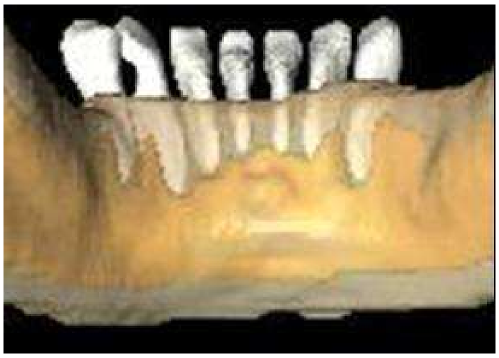

Figure 4: Dental anatomy and its realisation within our project.

Our main focus was an analysis of stress/strain profiles of the mandibular ramus. Therefore, we neglected the complicated dental anatomy, especially the periodontal ligament between bony tissue and teeth, see Figure 4 (left), and the so-called lamina dura which is a thin cortical hull around the periodontal ligament. For the sake of similarity with the cortical lamina dura, within our model, the teeth were embedded into an alveole consisting also of cortical bone, see Figure 4 (right).

The condyles were embedded into simplified temporo mandibular joint capsules where they are freely mobile. The capsules' bonding to the skull was modeled by rigid attachment, see Figure 5. According to [15], we chose E = 20 MPa for the temporo mandibular joint capsules. The Poisson ratio was set to $\nu = 0.3$.

As already mentioned in Section 1, the four respectively eight common mas-

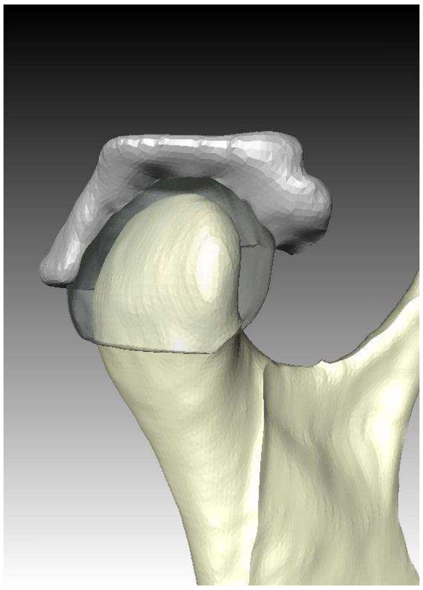

Figure 5: Realisation of the temporo mandibular joint: the condyles were freely mobile in a simplified joint capsule.

ticatory muscles were included in the simulation. These are the masseter muscles, the temporals, the medial, and lateral pterygoids, see Figure 6. Concerning the muscles we have to define the following features as necessary input of the simulation:

- appropriate muscular force values,
- more or less correct muscle attachments, and
- the directions of muscles' activity, the so-called lines of action.

Traditionally, see [23], muscular force values are related to their cross sectional area. Instead, we refer to data based on electromyographic measurements, see [22]. For the muscle attachments, we refer to the results of – in the case of soft tissue still tedious – segmentation of the CT data and subsequent surface reconstruction. Finally, the reconstruction of highly resolved vector fields of individual lines of action is subject of this article, see the procedure described in Subsection 2.3. It was performed by means of a volumetric visualization of the muscle's inner structure based on CT– or MRT–data. Its impact on stress/strain profiles of the mandible is studied in Section 3.

In [18], a method is described to estimate the individual line of action of a muscle from serial images of parallel muscle cross sections obtained in vivo

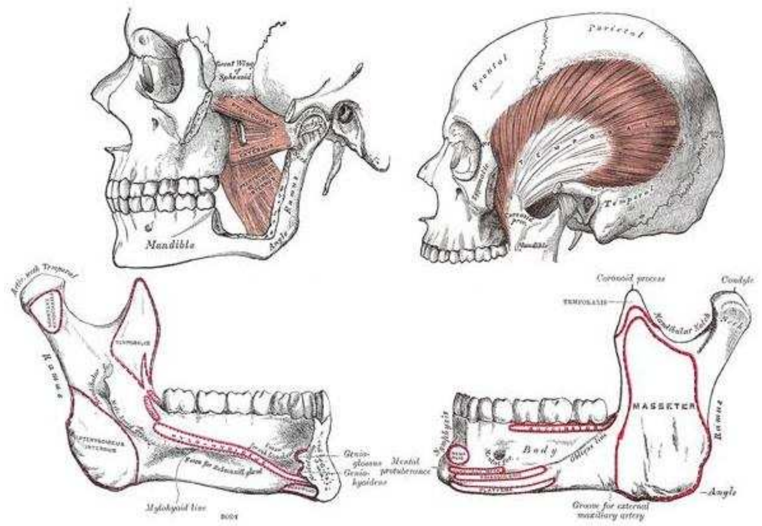

Figure 6: The masticatory system consisting of the masseter muscles, the temporals, the medial, and the lateral pterygoids [10].

by means of CT or MRI scanning. By this method, the "central line" of the external shape of the muscle is going to be reconstructed. So, the result is individual but not related to the muscle's inner structure.

Another approach for individual, but in vitro, reconstruction of muscle attachments and lines of action combined with subsequent finite element simulation was presented by Pleschberger [21]. During sequential dissection of the mandible, he marked the muscles by thin wires and took X–ray–images of the preparation with the wires from two orthogonal directions. So, he could identify special lines of action according to the wires.

Korioth et al. [19] referred for the muscular lines of action they applied within their simulations to the work of Baron and Debussy [4]. Based on an analysis of five cadaver heads, Baron and Debussy defined an ensemble of 12 fascicles on each side: four "vectors" for the fascicles of the masseter muscle, three for the temporal, three for the medial pterygoid, and two for the lateral pterygoid. Of course, this approach is very sophisticated but not individual.

2.2 Numerical background: adaptive finite elements

To study our human mandible, we consider the three–dimensional Navier–Lamé equations of linear elasticity

$$
\begin{aligned}
-2\,\mu\,\mathrm{div}\,\epsilon(\boldsymbol{u}) - \lambda\,\mathrm{grad}\,\mathrm{div}\,\boldsymbol{u} &= \boldsymbol{f} \quad \text{in } \Omega & (1)\\
(\lambda\,\mathrm{tr}(\epsilon(\boldsymbol{u}))I + 2\,\mu\,\epsilon(\boldsymbol{u}))\cdot\boldsymbol{n} &= \boldsymbol{g} \quad \text{on } \Gamma_N & (2)\\
\boldsymbol{B}\cdot\boldsymbol{u} &= \boldsymbol{d} \quad \text{on } \Gamma_D & (3)
\end{aligned}
$$

where $\boldsymbol{u} = (u_1, u_2, u_3)^T$ denotes the displacement vector and $\epsilon(\boldsymbol{u}) := (\nabla\boldsymbol{u} + (\nabla\boldsymbol{u})^T)/2$ is the strain tensor. We assume that the computational domain $\Omega \subset \mathbb{R}^3$ is a bounded Lipschitz domain with polygonal boundary Γ. Neumann and Dirichlet boundary conditions are given on $\Gamma_N \subset \Gamma$ and $\emptyset \neq \Gamma_D \subset \Gamma$, respectively. The physical values λ and μ are the Lamé constants which are related to Young's modulus E and Poisson's number ν by

$$
\mu = \frac{E}{2\,(1+\nu)} \quad \text{and} \quad \lambda = \frac{E\,\nu}{(1+\nu)(1-2\nu)}\,.
$$

We impose the following regularity assumptions:

$$
\boldsymbol{f} \in [L^2(\Omega)]^3,\ \boldsymbol{B} \in [L^\infty(\Gamma_D)]^{3\times 3},\ \boldsymbol{d} \in [H^1(\Omega)]^3,\ \text{and } \boldsymbol{g} \in [L^2(\Gamma_N)]^3\,.
$$

Then, we seek for a weak solution $\boldsymbol{u} \in [H^1(\Omega)]^3$ such that $\boldsymbol{B}\cdot\boldsymbol{u} = \boldsymbol{d}$ on Γ_D and for all $\boldsymbol{v} \in V := \{\boldsymbol{v} \in [H^1(\Omega)]^3 : \boldsymbol{B}\cdot\boldsymbol{v} = 0 \text{ on } \Gamma_D\}$,

$$
\int_\Omega \epsilon(\boldsymbol{v}) : \mathbb{C}\ \epsilon(\boldsymbol{u})\, d\boldsymbol{x} = \int_\Omega \boldsymbol{f}\cdot\boldsymbol{v}\, d\boldsymbol{x} + \int_{\Gamma_N} \boldsymbol{g}\cdot\boldsymbol{v}\, ds\,. \tag{4}
$$

Here, $\mathbb{C}$ is the isotropic material tensor. Defining the Voigt representation $\gamma(\boldsymbol{u}) : [H^1(\Omega)]^3 \to [L^2(\Omega)]^6$ of the linear Green strain tensor

$$
\gamma(\boldsymbol{u}) = (\epsilon_{11}(\boldsymbol{u}), \epsilon_{22}(\boldsymbol{u}), \epsilon_{33}(\boldsymbol{u}), 2\epsilon_{12}(\boldsymbol{u}), 2\epsilon_{13}(\boldsymbol{u}), 2\epsilon_{23}(\boldsymbol{u}))^T
$$

and using the relation

$$\begin{pmatrix} \sigma_{11} \\ \sigma_{22} \\ \sigma_{33} \\ \sigma_{12} \\ \sigma_{13} \\ \sigma_{23} \end{pmatrix} = \frac{E}{(1+\nu)(1-2\nu)} \begin{pmatrix} 1-\nu & \nu & \nu & 0 & 0 & 0 \\ \nu & 1-\nu & \nu & 0 & 0 & 0 \\ \nu & \nu & 1-\nu & 0 & 0 & 0 \\ 0 & 0 & 0 & \frac{1-2\nu}{2} & 0 & 0 \\ 0 & 0 & 0 & 0 & \frac{1-2\nu}{2} & 0 \\ 0 & 0 & 0 & 0 & 0 & \frac{1-2\nu}{2} \end{pmatrix} \begin{pmatrix} \epsilon_{11} \\ \epsilon_{22} \\ \epsilon_{33} \\ \epsilon_{12} \\ \epsilon_{13} \\ \epsilon_{23} \end{pmatrix}$$

$$=: \; \mathcal{C}\gamma(\boldsymbol{u})$$

for the components of the stress tensor, we obtain

$$\epsilon(\boldsymbol{v}) : \mathbb{C}\ \epsilon(\boldsymbol{u}) = \gamma^T(\boldsymbol{v})\mathcal{C}\gamma(\boldsymbol{u})\,.$$

For reasonable boundary conditions, the well–known Lax–Milgram Lemma and Korn's inequality yield the existence and uniqueness of a weak solution $\boldsymbol{u}$ in (4).

The weak formulation (4) is the starting point for our finite element method. Let Ω_h be a permissible triangulation of Ω into tetrahedra and let S_h^1 be the standard finite element space of piecewise linear continuous vector functions. The finite element solution $\boldsymbol{u}_h \in S_h^1$ has then to satisfy $\boldsymbol{B} \cdot \boldsymbol{u}_h = \boldsymbol{d}_h$ on Γ_D, where $\boldsymbol{d}_h$ is the projection of $\boldsymbol{d}$ onto S_h^1, and for all $\boldsymbol{v}_h \in S_h^1$ with $\boldsymbol{B} \cdot \boldsymbol{v}_h = 0$ on Γ_D

$$\int_\Omega \epsilon(\boldsymbol{v}_h) : \mathbb{C}\ \epsilon(\boldsymbol{u}_h)\, d\boldsymbol{x} = \int_\Omega \boldsymbol{f} \cdot \boldsymbol{v}_h \, d\boldsymbol{x} + \int_{\Gamma_N} \boldsymbol{g} \cdot \boldsymbol{v}_h \, ds\,. \tag{5}$$

After computing the discrete displacement vector $\boldsymbol{u}_h$ by the preconditioned cg-method [12], we derive a posteriori error estimation from a hierarchical decomposition, compare [7, 6]. Let $S_h^2 = S_h^1 \oplus Z_h^2$ with Z_h^2 being the finite dimensional space of piecewise quadratic functions that are necessary to enrich the space S_h^1 to the standard finite element space S_h^2 of continuous piecewise quadratic functions. Note the degrees of freedom represented by the basis functions of Z_h^2 are located in the midpoints of the edges of the triangulation Ω_h. An approximation $\boldsymbol{e}_h \in Z_h^2$ of the finite element error $\boldsymbol{u} - \boldsymbol{u}_h$ can be computed from

$$\int_\Omega \epsilon(\boldsymbol{\phi}_h) : \mathbb{C}\ \epsilon(\boldsymbol{e}_h)\, d\boldsymbol{x} = \int_\Omega \boldsymbol{f}\cdot\boldsymbol{\phi}_h - \epsilon(\boldsymbol{\phi}_h) : \mathbb{C}\ \epsilon(\boldsymbol{u}_h)\, d\boldsymbol{x} + \int_{\Gamma_N} \boldsymbol{g}\cdot\boldsymbol{\phi}_h\, ds \tag{6}$$

$$\boldsymbol{B}\cdot\boldsymbol{e}_h = \boldsymbol{\omega}_h \quad \text{on } \Gamma_D \tag{7}$$

for all $\boldsymbol{\phi}_h \in Z_h^2$ with $\boldsymbol{B}\cdot\boldsymbol{\phi}_h = 0$ on Γ_D. Here, $\boldsymbol{\omega}_h \in Z_h^2$ denotes the Z_h^2–part of the projection of $\boldsymbol{d}$ onto S_h^2. A simplified version of this error estimator is obtained replacing the bilinear form on the left–hand side by its block–diagonal approximation over Z_h^2. Let

$$(\boldsymbol{\phi}_1,\dots,\boldsymbol{\phi}_{3N}) = (\eta_1\boldsymbol{e}_1, \eta_1\boldsymbol{e}_2, \eta_1\boldsymbol{e}_3, \eta_2\boldsymbol{e}_1, \dots, \eta_N\boldsymbol{e}_3)$$

be the nodal basis of the space Z_h^2, where N is the number of edges of Ω_h and η_i is the scalar piecewise quadratic function of edge–node m_i, i.e., $\eta_i(m_i) = 1$ and $\eta_i(z) = 0$ for all other nodes z in the triangulation Ω_h. For the discrete error vector, we have

$$\boldsymbol{e}_h = \sum_{i=1}^{3N} e_{h,i}\,\boldsymbol{\phi}_i$$

and thus the coefficient of the global stiffness matrix $A = (a_{kl})$ in (6) are defined as

$$a_{kl} = \int_\Omega \epsilon(\boldsymbol{\phi}_k) : \mathbb{C}\ \epsilon(\boldsymbol{\phi}_l)\, d\boldsymbol{x}\,, \quad k,l = 1,\dots,3N\,.$$

Its block–diagonal approximation reads

$$\tilde{A} = \begin{pmatrix} a_{11} & a_{12} & a_{13} & 0 & 0 & 0 & \cdots & 0 & 0 & 0 \\ a_{21} & a_{22} & a_{23} & 0 & 0 & 0 & \cdots & 0 & 0 & 0 \\ a_{31} & a_{32} & a_{33} & 0 & 0 & 0 & \cdots & 0 & 0 & 0 \\ 0 & 0 & 0 & a_{44} & a_{45} & a_{46} & \cdots & 0 & 0 & 0 \\ 0 & 0 & 0 & a_{54} & a_{55} & a_{56} & \cdots & 0 & 0 & 0 \\ 0 & 0 & 0 & a_{64} & a_{65} & a_{66} & \cdots & 0 & 0 & 0 \\ & & & & & & \ddots & & & \\ 0 & 0 & 0 & 0 & 0 & 0 & \cdots & a_{3N-2,3N-2} & a_{3N-2,3N-1} & a_{3N-2,3N} \\ 0 & 0 & 0 & 0 & 0 & 0 & \cdots & a_{3N-1,3N-2} & a_{3N-1,3N-1} & a_{3N-1,3N} \\ 0 & 0 & 0 & 0 & 0 & 0 & \cdots & a_{3N,3N-2} & a_{3N,3N-1} & a_{3N,3N} \end{pmatrix}$$

Replacing A by $\tilde{A}$ reduces the global computation of $\boldsymbol{e}_h$ to the computation of N small 3×3 linear systems which can be solved independently to get an approximation $\tilde{\boldsymbol{e}}_h$. This leads to a very efficient algorithm for computing a posteriori error estimators (see also [7, 6, 20]). The values

$$\eta_T := \left(\int_\Omega \epsilon(\tilde{\boldsymbol{e}_h}) : \mathbb{C}\ \epsilon(\tilde{\boldsymbol{e}_h})\ d\boldsymbol{x} \right)^{1/2}$$

can now serve as local error estimators and can be used to steer an adaptive refinement of the mesh. In Figure 7 we show the effect of three steps of adaptive refinement.

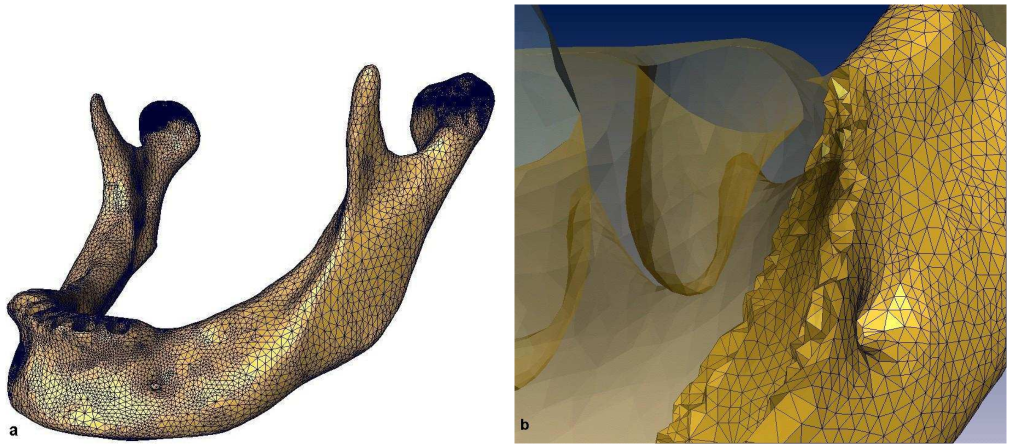

Figure 7: Adaptive grid refinement: a: finite element mesh of the mandible (level 3, about 740.000 tet.), b: view into the finite element mesh near the biting tooth.

The numerical algorithms described in this subsection are implemented in the code KASKADE [2, 8] which we used to get all the simulation results.

2.3 Highly resolved modelling of individual muscle activity

There is considerable variation in the arrangement of the fibres of certain muscles with reference to the tendons to which they are attached. In some muscles the fibres are parallel and run directly from their origin to their insertion. For those muscles parallel vectors might be a good approximation of its traction. For more details, see for instance [10].

In the contrary, the masticatory muscles are composed of fibres showing rather heterogeneous activity [5, 26]. Therefore, their functionality cannot be captured by groups of parallel vectors in only one direction.

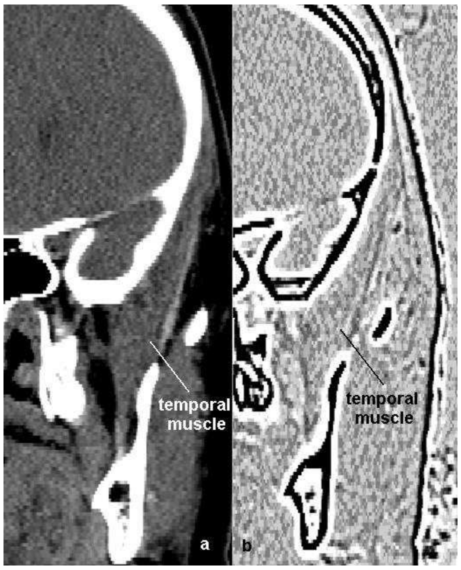

Figure 8: Coronal view of original and filtered CT–slice.

On the other, hand the muscles are coherent structures with inhomogeneous, but continuous fibre orientation, see the photograph of the anatomical preparation in Figure 13. You find a detailed discussion in [23].

Motivated by this observation, we want to deduce three dimensional inhomogeneous vector fields representing the individual lines of action of the masticatory muscles. The procedure consists of six steps and is exemplarily described for the temporal muscle. It can be realized in the same way for other muscles, see the examples at the end of this subsection.

Step 1: Especially for CT data of reduced quality, segmentation of soft muscular tissue is tedious and imprecise. Therefore, the first step consists in image processing of the CT data. By special filtering techniques, the bony contours were returned as dark lines enlaced by white edges of high grey value, see Figure 8. For muscular tissue, the situation is changed. But, nevertheless, the contour of the temporal muscle can be recognized in the filtered data set.

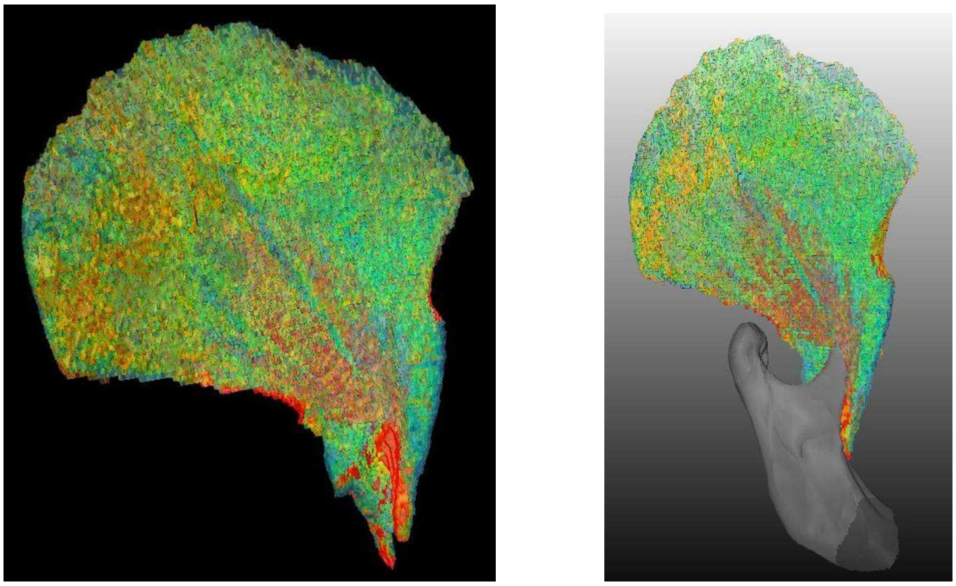

Figure 9: Visualization of the inner structure of the temporal muscle.

Step 2: By the preprocessing within the last step, improved segmentation of the muscles and their attachments is possible. For the result of the subsequent surface reconstruction, we refer to Figure 3.

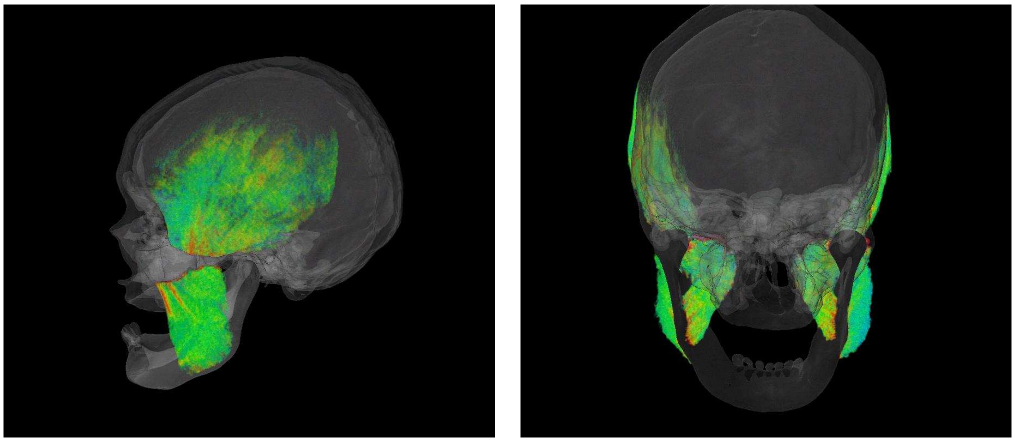

Figure 10: Visualization of the masticatory muscles by modified volume rendering.

Step 3: Having once succeeded in the segmentation of the muscles, we can apply the techniques described in [17], see also Figure 2. By this, a qualitative profile of the inner structure of the considered muscle can be given, see Figure 9. These methods are very hardware intensive.

About two millions of little faces have to be rendered. A less extensive representation can be given by modified volume rendering, see Figure 10. Now, all masticatory muscles can be rendered simultaneously.

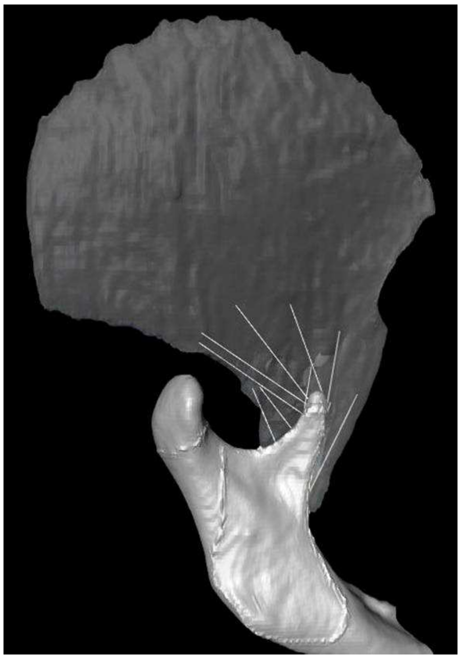

Figure 11: “guiding lines” related to the individual directions of tendons and fibres.

Step 4: In the profile of the inner structure of the last step, it is possible to select “guiding lines” related to tendons and fibres, see Figure 11. For further processing the guiding lines are normalized.

In the case of data based on magnetic resonance imaging (MRI), the tendons up to the basic course of the fibres can be visualized, see [14]. The in principle better soft tissue representation by MRI is rigorous. But in our actual example, the applicability of this method also to CT-data of standard quality is demonstrated.

Step 5: In this step, the lines of action starting from arbitrary points within the muscle attachment are calculated as linear combinations of the guiding lines.

We claim that a guiding line $\vec{f_1}$ “insulates” a point P from another guiding line $\vec{f_2}$ if line $\vec{f_2}$ lies in the rear hemisphere orthogonal to the connecting line between P and the starting point of line $\vec{f_1}$. Only the not insulated guiding lines are admitted to an interpolation with weights inversely proportional the nth power of the distance to P with an positive integer n. By this, we avoid that the fibres at the muscle's posterior portion influence the lines of action at the anterior one and vice versa.

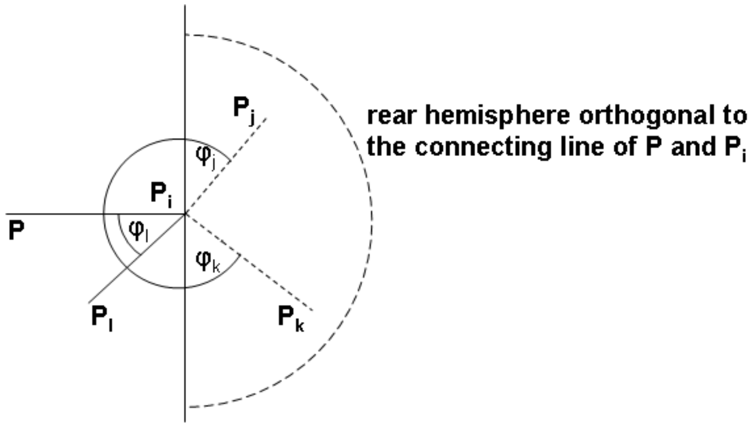

Figure 12: The guiding line starting at P_i "insulates" the guiding lines starting at P_j and P_k because the angles ϕ_j, ϕ_k are greater than 90^o. Accordingly, the guiding line starting at P_l is not insulated.

In detail, let us consider the points $P_1, ..., P_n$ as the starting points of the guiding lines $\vec{f}_1, ..., \vec{f}_n$. P may be an arbitrary point inherent to the muscle attachment. The appropriate line of action $\vec{f}_P$ at P will be defined as a weighted linear combination of the guiding lines $\vec{f}_1, ..., \vec{f}_n$:

$$\vec{f}_P = \sum_{i=1}^{n} w_i \, a_i \, \vec{f}_i,$$

where

a) $w_i = 0$, if the line $\vec{f}_i$ at P_i is insulated from $\vec{f}_P$ by another line $\vec{f}_j$. This means that the angle ϕ between the connecting line PP_j and the connecting line P_jP_i is greater than 90^o, see also Figure 12. Otherwise $w_i = 1$.

b) The value a_i is set proportional to $||\vec{f}_P - \vec{f}_i||^n$ with an positive integer n. The sum over all $a_i w_i$ is normalized to 1.

Short comment on the choice of the exponent n: with increasing n, the weights of the near guiding lines are also increasing. We aim at a continuous vector field. By visual inspection and comparison with the anatomical preparations, $n = 3$ proved to be a good choice. See Subsection 3.2 for a sensitivity analysis with respect to this exponent.

c) Finally, the vector $\vec{f_P}$ is scaled to a unit vector.

Step 6: This step is dedicated to the assignment of values of force density to the unit vectors $\vec{f_P}$ obtained in Step 5. The physical unit is N/m^2. The easiest way is a homogeneous force density, for instance referring to a force value found by experimental evidence divided by the area of the muscle attachment. A more physiological approach is compartmentalisation based on the results of electromyographic measurements as [22] or anatomical literature, see for instance the detailed discussion in [23]. By this, an inhomogeneous force density is obtained.

Figure 13: Juxtaposition of the calculated lines of action of the temporal muscle and a real preparation (preparation: Anatomische Anstalt, Univ. of Munich, photograph: C. Kober).

For first results and a comparison with a real preparation, see the Figure 13. Within the finite element analysis of the mandible, these muscular lines of action serve as Cauchy boundary conditions at their insertion. Therefore, the curvature of the fibres within the muscle itself has not to be taken into account. For a first attempt of the group involving also the muscular tissue itself, see [14]. There, the inherent curvature of the lines of action has been taken into account. See also Section 4.

We want to add some comments concerning our ansatz of insulated points in Step 5. With a view to the right picture of Figure 13, a muscle consists of a large but finite number of fibres and tendons. The fibres are not infinitely small, but they show finite radial dimensions. Together, they form a coherent organ, namely the muscle, in the contrary to a continuous force field, a radiation field for instance. Our guiding lines are chosen as representative in the sense that the neighbouring fibres – and only those – are very similar. By this, it may be justified to compute the other fibres by weighted interpolation. An alternative ansatz might be looking at the guiding lines as sources of forces with an exponentially decreasing influence sphere. This would correspond to the "radiation field philosophy". In our opinion this approach is not physiological.

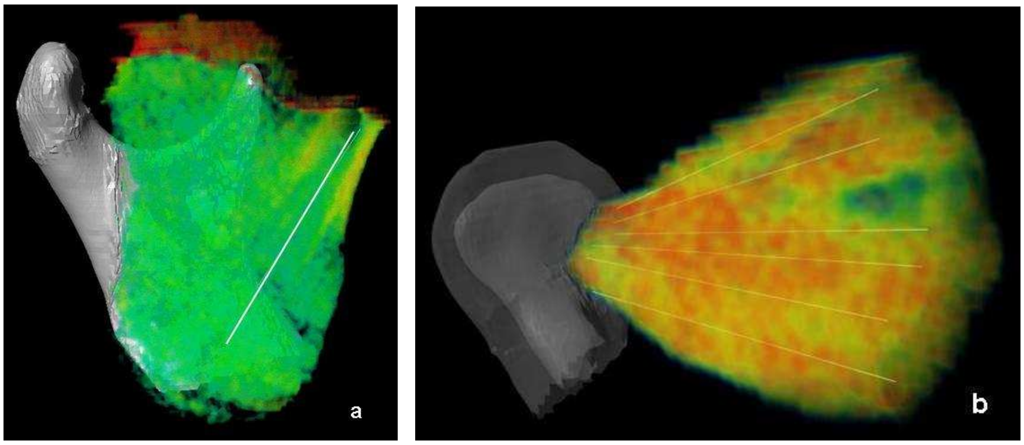

Figure 14: Visualization of the masseter (a) and of the lateral pterygoid muscle (b).

Comparable processing for the other masticatory muscles, as the masseter muscle or the lateral ptergygoid, has already been performed or is in progress, see Figures 14a and b.

3 Results

3.1 Simulation results

As an example, we simulate a lateral bite on the leftmost premolar. Our interest is focused on the mandibular ramus. The biting tooth assumed as nearly not deformable is pressed by muscle forces towards a very hard object to be crunched. Therefore, within this stage of our project, we keep this tooth fixed. The other teeth are freely mobile.

This setting can be compared with an orthogonal bite on a very hard metallic pencil. This choice was motivated by the demand of an asymmetric and, at the same time, extreme test case.

	masseter	temporalis	pteryg. medialis	pteryg. lateralis
force, biting side [N]	91	81	43	0
force, balancing side [N]	60	68	29	0
area of muscle attachment biting side $[m^2]$	1.1305e-3	4.4949e-4	3.2430e-4	7.4849e-5
area of muscle attachment balancing side $[m^2]$	1.1245e-3	4.0823e-4	3.2610e-4	8.8882e-5
force density, biting side $[\mathrm{N}/m^2]$	8.0495e+4	1.8020e+5	1.3259e+5	0
force density, balancing side $[\mathrm{N}m^2]$	5.3357e+4	1.6657e+5	8.8930e+4	0

Table 1: Muscular forces according to [22].

As reported in the previous sections, the four respectively eight common masticatory muscles were included in the simulation. For muscular force density, we refer to the data given in [22] based on electromyographic measurements divided by the area of the respective muscle attachment, see Table 1. We applied inhomogeneous vector fields of lines of action as derived in Subsection 2.3. But, for want of appropriate input data, we refrained from compartmentalisation.

Because of its significance in bone adaptation, we discuss the simulation results with respect to the volumetric strain ϵ being the trace of the strain tensor ϵ_{ij}. Figure 15 shows the result of the numerical computation.

The impact of the posterior portion of the temporal muscle is illustrated in Figure 16, see also [15]. The photography of an anatomical preparation shows the formation of the fibres of this muscles. We juxtaposed the simulation results (volumetric strain, von Mises equivalent stress) and two different representations of the density profile which are modified volume rendering and the methods described in [17]. As discussed in [15], the marked small spot of reduced density within the incisura corresponds to elevated compression, see the profile of volumetric strain, resp. elevated von Mises equivalent stress. Inter alia, this agreement motivated our actual study.

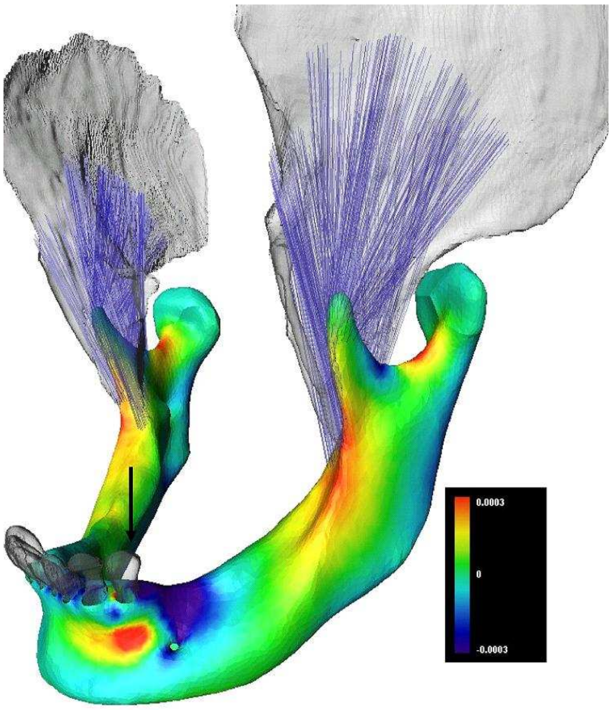

Figure 15: Simulation result: volumetric strain due to a bite on the leftmost premolar.

3.2 Sensitivity analysis

In this context, we performed two approaches of sensitivity analysis. First, we analysed the impact of adaptive grid refinement at the mandibular ramus. Second, we tested the volumetric strain profile with respect to the realisation of the temporal muscle.

In a first sensitivity analysis, we performed simulations with the fully refined setting as given in Subsection 3.1. The number of tetrahedra was more than quadrupled from level 0 to level 2. Most notably, adaptive grid refinement occured at the temporo mandibular joint capsules and in the neighbourhood of the biting tooth. Within this work, we focus on the mandibular ramus (esp. at the working side) and compare the volumetric strain profiles from level 0, level 1, and level 2, see Figure 17. In this context, visual inspection does not reveal any qualitative changes, neither at the working nor at the balancing side. Next, we analyse the quantitative changes between the levels. For a local comparison, we transferred the results of a level 1 computation for instance to a level 0 grid and calculated the difference. At the rami, this difference for the level 0 and the level 1 simulation is about 10^{-5}. This value

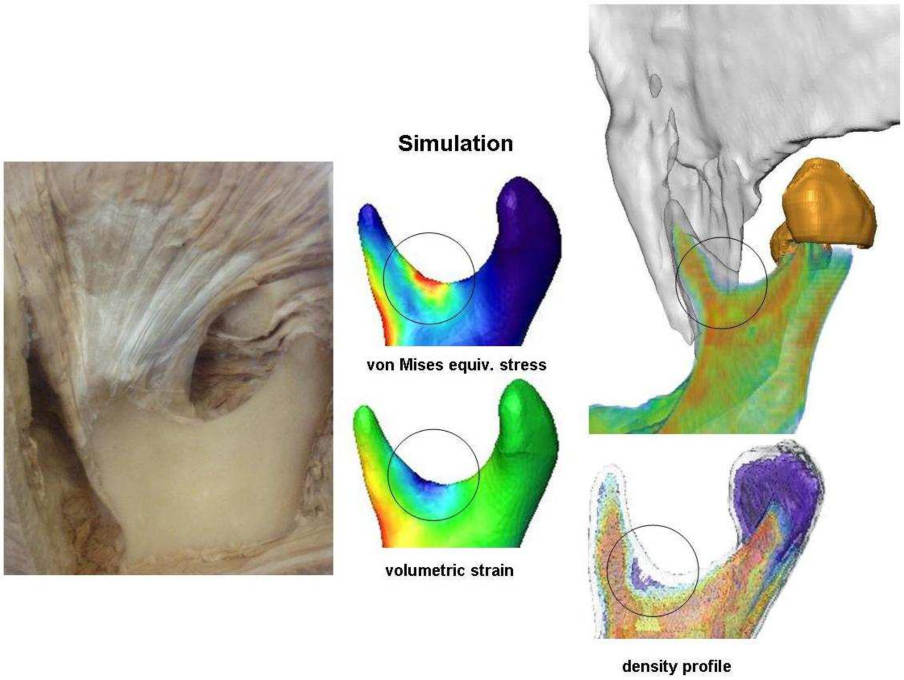

Figure 16: Impact of the posterior portion of the temporal muscle (preparation: Anatomische Anstalt, Univ. of Munich, photograph: C. Kober).

is exceeded at the chin, near the biting tooth. Compared to an order of magnitude of 10^{-4} of the strain itself, we decided to proceed to higher levels. In the lower right picture of Figure 17, the difference between a computation of volumetric strain at level 1 and at level 2 is shown. This difference profile exhibits high values at the mandibular condyles where we also can state high rate of adaptive grid refinement. In the contrary, at the both rami, its order of magnitude is less than 10^{-6}. The order of magnitude of the unmodified strain results is 10^{-4}. So, one might estimate that the relative error due to finite element discretisation at the mandibular rami has order of magnitude 10^{-2} which is very small compared to other sources of imprecision inherent to our simulation. Thus we can rely on the accuracy of the level 1 results for all further considerations in this paper.

Next, we consider the variances of the strain profile due to different realisation of the temporal muscle. For some examples, see Figure 18. Based on the level 2 results, we tested the following settings:

1: Homogeneous muscular traction over the whole muscle:
   a) aligned to the anterior portion of the temporal muscle,
   b) parallel to the coronoid process, see also Figure 18,

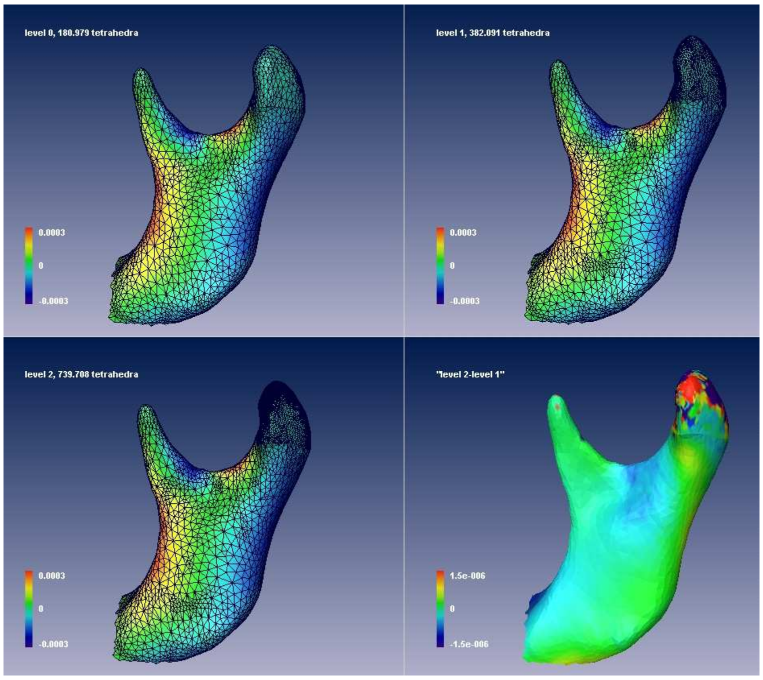

Figure 17: Sensitivity analysis with respect to adaptive grid refinement: working side (volumetric strain).

c) aligned to the posterior portion of the temporal muscle.

2: Two guiding lines:
We chose the first guiding line according to the anterior portion of the temporal muscle,
the second one according to its posterior portion.
The interpolation is done by the nearest neighbour method, in which the fibre closest to a point is the line of action in that point. See also Figure 18.

3: Guiding lines according to Step 4 of Subsection 2.3, see also Figure 11, but interpolation performed by the nearest neighbour method.

4: Guiding lines vectors according to Step 4 of Subsection 2.3, see Figure 11, interpolation as descibed in Step 5 with different choice of the parameter n:
a) $n = 1$
b) $n = 2$
c) $n = 3$, see also Figure 18.
By comparison with the real preparations, the case "$n = 3$" proved best to fit with reality.

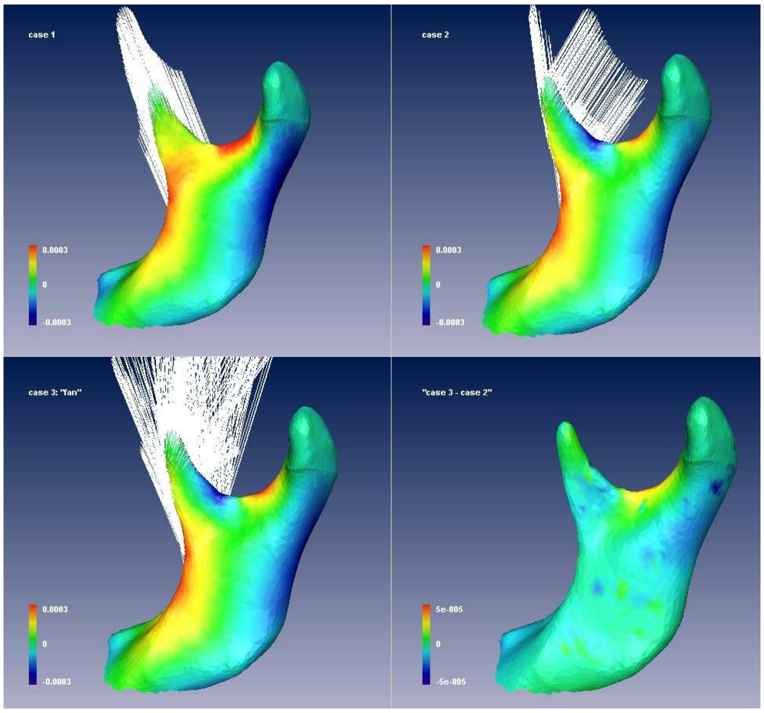

Figure 18: Sensitivity analysis with respect to different realisation of the temporal muscle: working side (volumetric strain).

As expected, the cases of Setting 1 showed decisive qualitative differences compared to the simulation results based on the fully refined input data described in the preceding subsection. The case of Setting 1b is displayed in the top left picture of Figure 18. The direction of traction was set parallel to the coronoid process. As expected, this test case did not exhibit the little spot of compression discussed already in the last section, see Figure 16.

The results of the other settings did not reveal such striking differences. The volumetric strain related to Setting 2 is depicted top right in Figure 18. The realisation of the temporal is based on two guiding lines, the first one aligned to the strong anterior portion of the muscle, the other aligned to its posterior portion. The full fanlike reconstruction, Setting 4c, can be seen bottom left in Figure 18. The calculated difference between the strain profile due to this full fanlike reconstruction and the one due to Setting 2 is given in Figure 18, bottom right. Its order of magnitude is about 10^{-5}, while the unmodified strain results have an order of magnitude of 10^{-4}. So we have to realize a relative error of about 10%.

Inter alia, the positive values (yellow colour) of the difference profile at the neck of the condyle indicate that the strain values of the fully refined reconstruction (Setting 4c) are higher than those due to Setting 2. So, the Setting 4c is more similar to the density profile depicted in Figure 2 and therefore in some sense more physiological.

The results within Setting 4 differ about 1%. The choice for $n = 3$ as the best case was done by a comparison of the reconstructed vector fields with the arrangement of the fibres of some anatomical preparations, see for instance Figure 13.

4 Conclusion and outlook

We presented a new approach of muscular modelling in the context of adaptive finite element simulation involving the individual fine structure of the muscles.

Using adaptive grid refinement the numerical method provided reliable results. The difference of about 1% between the results of level 2 calculations and corresponding level 1 calculations ensured that the discretisation error is less than the errors caused by the modelling.

The simulation results showed qualitative impact of the physiological modelling of muscular forces, see the comparison depicted in Figure 16 and the respective sensitivity analysis in the preceding subsection. This sensitivity analysis revealed a difference of about 10% between the results of a realisation of the temporal muscle based on two guiding lines and the fanlike reconstruction which is the particular subject of this article. In the contrary to standard engineering simulation, a variance of this order of magnitude is not exorbitant compared to other sources of imprecision.

An appropriate algorithm for the assignment of more or less individual force density values to special "compartments" of the muscles, see Step 6 of our modeling procedure in Subsection 2.3, is subject of ongoing work. First tests showed reliable results.

A sensitivity analysis with respect to the muscle attachment of the masseter muscle revealed best agreement with the density profile of Figure 2 for that muscle attachment which corresponds best to reality given by the CT–data. This result may be interpreted as further tessera for our approach stated at the beginning, see Section 1 or [15].

As mentioned in Subsection 2.3, the muscular lines of action serve within the framework of the mandible simulation as Cauchy boundary conditions mainly at their insertion. Therefore, the course of the fibres and tendons inside the muscle is not relevant. In [14], an extension of the presented ansatz is given towards an anisotropic reconstruction of the muscular tissue, see Figure 19.

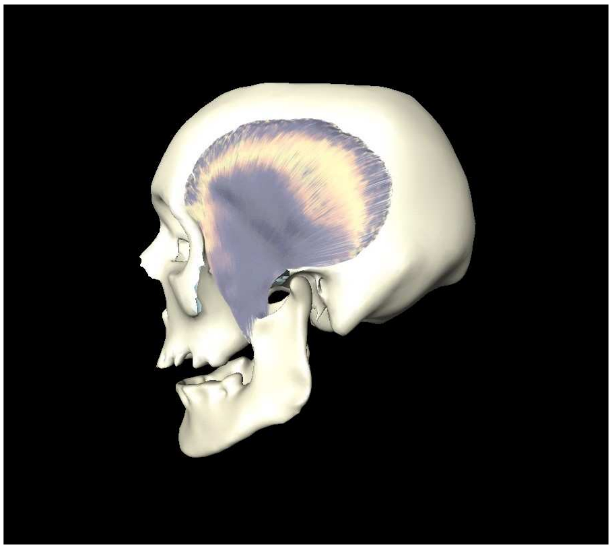

Figure 19: Anisotropic reconstruction of a human temporal muscle, see [14].

5 Acknowledgement

The authors address their best thanks to Jürgen Lenz, University of Karlsruhe, for his cooperation in the field of craniofacial and dental simulation and also for drawing their attention to the GAMM–Meeting in March 2004 in Dresden.

Furthermore, we want to express our sincere appreciation to Peter Deuflhard, Zuse Institute Berlin, who provided the numerical platform for our FEM simulation and gave support in many fruitful discussions.

For his help concerning the photographs of the anatomical dissections, we acknowledge Volker Kuhn, Anatomische Anstalt, University of Munich.

The first author wants to thank the "Amira–group" at the Zuse Institute, especially Hans–Christian Hege and Detlev Stalling, for the license of Amira 3.1. All reported visualizations have been performed with Amira [1, 24].

References

[1] http://www.amiravis.com

[2] http://www.zib.de/SciSoft/kaskade

[3] National Library of Medicine. The Visible Human Project, http://www.nlm.nih.gov/research/visible/visible_human.html, 1995.

[4] P. Baron, T. Debussy: A Biomechanical Functional Analysis of the Masticatory Muscles in Man, Archs. Oral. Biol. 24 (1979), pp. 547-553.

[5] N.G. Blanksma, T.M. van Eijden, L.J. van Ruijven, W.A. Weijs: Electromyographic heterogeneity in the human temporalis and masseter muscles during dynamic tasks guided by visual feedback, J Dent Res. 1997, 76(1), pp. 542-551.

[6] F. Bornemann, B. Erdmann, R. Kornhuber: Adaptive multilevel–methods in three space dimensions, Int. J. Num. Meth.in Eng, Vol. 36, (1993), pp. 3187-3203.

[7] P. Deuflhard, P. Leinen, H. Yserentant: Concepts of an Adaptive Hierarchical Finite Element Code. IMPACT Comp. Sci. Eng. 1 (1989), pp. 3-35.

[8] B. Erdmann, J. Lang, R. Roitzsch: KASKADE–Manual, Technical Report TR 93-05, Konrad–Zuse–Zentrum Berlin (ZIB), 1993.

[9] B. Erdmann, C. Kober, J. Lang, P. Deuflhard, H.-F. Zeilhofer, R. Sader: Efficient and Reliable Finite Element Methods for Simulation of the Human Mandible, Proceedings of 9th Workshop on The Finite Element Method in Biomedical Engineering, Biomechanics and Related Fields, CDRom, Ulm, Germany, July 2002.

[10] H. Gray: Anatomy of the Human Body, http://www.bartleby.com/107/.

[11] R.T. Hart, V.V. Hennebel, N. Thongpreda, W.C. van Buskirk, and R.C. Anderson: Modeling the Biomechanics of the Mandible: A Three-Dimensional Finite Element Study, J. Biomechanics, 25 (1992), pp. 261-286.

[12] M.R. Hestenes, E. Stiefel: Methods of Conjugate Gradients for Solving Linear Systems, J. Res. Nat. Bur. Stand. 49 (1952), pp. 409-436.

[13] C. Kober, B. Erdmann, C. Hellmich, R. Sader, H.–F. Zeilhofer: Anisotropic Simulation of the Human Mandible, accepted at EM2004, June 13-16, 2004, Univ. of Delaware, Newark, USA.

[14] C. Kober, R. Sader, H.–F. Zeilhofer: Anisotropic Reconstruction of the Human Masticatory Muscles, submitted to the Proc. of the BMT2004, Ilmenau, Sept. 2004.

[15] C. Kober, B. Erdmann, R. Sader, and H.F. Zeilhofer: Simulation (FEM) of the Human Mandible: A Comparison of Bone Mineral Density and Stress/Strain Profiles Due to the Masticatory System, in Proceedings 10th Workshop on The Finite Element Method in Biomedical Engineering, Biomechanics and Related Fields, Ulm, Germany, July 17-18, 2003.

[16] C. Kober, R. Sader, H.-F. Zeilhofer: Multimodal Preprocessing for Human Biting Simulation, Proceedings of 9th Workshop on The Finite Element Method in Biomedical Engineering, Biomechanics and Related Fields, CDRom, Ulm, Germany, July 2002.

[17] C. Kober, R. Sader, H.-F. Zeilhofer: Segmentation and visualization of the inner structure of craniofacial hard tissue, in Proc. Comp. Ass. Rad. Surg., London, Vol. 1256 (2003), pp. 1257-1262.

[18] J.H. Koolstra, T.M. van Eijden, W.A. Weijs: An iterative procedure to estimate muscle lines of action in vivo, J Biomech., 1989, 22(8-9), pp. 911-920.

[19] T.W. Korioth, D.P. Romilly, and A.G. Hannam: Three Dimensional Finite Element Stress Analysis of the Dentate Human Mandible, Am. J. of Phys. Anthr., 88 (1992), pp. 69-96.

[20] J. Lang: Adaptive Multilevel Solution of Nonlinear Parabolic PDE Systems, Lecture Notes in Computational Science and Engineering, Hrsg.: M. Griebel, D.E. Keyes, R.M. Nieminen, D. Roose, T. Schlick, Springer, 2000.

[21] M. Pleschberger: Integrated 3D CT-FE Modeling System for Stress Analysis of the Human Mandible, Dissertation, Tech. Univ. Wien, 1999.

[22] Q. Rong: Finite Element Simulation of the Bone Modeling and Remodeling Process around a Dental Implant, Ph.D. Thesis, Universität Karlsruhe, June 2002.

[23] G.H. Schumacher: Funktionelle Morphologie der Kaumuskulatur, Jena, Verlag VEBG Fischer 1961.

[24] D. Stalling, M. Westerhoff, H.-C. Hege: Amira – an objectoriented system for visual data analysis. In C. Johnson, C. Hansen (Eds.), Visualization Handbook, Academic Press, 2003.

[25] T.M. van Eijden: Biomechanics of the mandible, Crit Rev Oral Biol Med. 2000, 11(1), pp. 123-136.

[26] T.M. van Eijden, J.H. Koolstra, P. Brugman: Three-dimensional structure of the human temporalis muscle, Anat Rec. 1996, 246(4), pp. 565-572.

[27] J. Wolff: Das Gesetz der Transformation der Knochen, Hirschwald Berlin, 1892.